# An investigation of performance characteristics of a pixellated room-temperature semiconductor detector for medical imaging

## P Guerra[1], A Santos[1,2] and D G Darambara[3]

[1] Centro de Investigación Biomédica de Bioningeniería, Biomateriales y Nanomedicina, CEEI-Modulo 3, C/ María de Luna, 11, 50018 Zaragoza
[2] Dpto Ingeniería Electrónica, Universidad Politecnica de Madrid, E-28040 Madrid, Spain
[3] Joint Department of Physics, The Royal Marsden NHS Foundation Trust and The Institute of Cancer Research, Fulham Road, London SW3 6JJ, UK

E-mail: pguerra@ciber-bbn.es

## Abstract

The operation of any semiconductor detector depends on the movement of the charge carriers, which are created within the material when radiation passes through, as a result of energy deposition. The carrier movement in the bulk semiconductor induces charges on the metal electrodes, and therefore a current on the electrodes and the external circuit. The induced charge strongly depends on the material transport parameters as well as the geometrical dimensions of a pixellated semiconductor detector. This work focuses on the performance optimization in terms of energy resolution, detection efficiency and intrinsic spatial resolution of a room-temperature semiconductor pixellated detector based on CdTe/CdZnTe. It analyses and inter-relates these performance figures for various dimensions of CdTe and CdZnTe detectors and for an energy range spanning from x-ray (25 keV) to PET (511 keV) imaging. Monte Carlo simulations, which integrate a detailed and accurate noise model, are carried out to investigate several CdTe/CdZnTe configurations and to determine possible design specifications. Under the considered conditions, the simulations demonstrate the superiority of the CdZnTe over the CdTe in terms of energy resolution and sensitivity in the photopeak. Further, according to the results, the spatial resolution is maximized at high energies and the energy resolution at low energies, while a reasonable detection efficiency is achieved at high energies, with a $1 \times 1 \times 6 \, mm^3$ CdZnTe pixellated detector.

(Some figures in this article are in colour only in the electronic version)

## 1. Introduction

In the last decade, there has been a rapidly increasing interest in room-temperature semiconductor detectors of high atomic number Z, such as CdTe and CdZnTe (CZT), supported by recent advances in the crystal growth and device fabrication techniques. High resistivity CdTe/CdZnTe semiconductors, suitable for x-ray and gamma-ray detectors, have been successfully grown by various growth techniques (Raiskin and E Butler 1988, Johnson *et al* 1993, Palosz *et al* 1995,

Eisen and Shor 1998, Szeles and Eissler 1998, Funaki *et al* 1999, Li *et al* 2003, Szeles 2004). However, several technical aspects that govern the charge carrier transport and device performance, such as material defects (e.g. polycrystallinity and inhomogeneity) and structural defects, still remain unresolved posing significant challenges, and thus preventing the large scale utilization of the material. Nevertheless, a lot of efforts have been directed towards understanding and improving both material quality and performance of CdTe/CZT semiconductors.

**Table 1.** Main physical properties of Si, Ge, CdTe and CdZnTe semiconductors.

| Material | Si | Ge | CdTe | CdZnTe |
|---|---|---|---|---|
| Atomic Number | 14 | 32 | 48,52 | 48,30,52 |
| Band Gap (eV) | 1.12 | 0.74 | 1.50 | 1.572 |
| Energy per e–h (eV) | 3.62 | 2.96 | 4.43 | 4.64 |
| Fano Factor | 0.14 | 0.08 | 0.06 (Owens and Peacock 2004) 0.2 (Lutz 1999) | 0.1 |
| $\mu_e$ (cm$^2$ V$^{-1}$ s$^{-1}$) | 1400 | 3900 | 1100 | 1000 |
| $\mu_h$ (cm$^2$ V$^{-1}$ s$^{-1}$) | 1900 | 1900 | 100 | 50–80 |
| $\tau_e$ (s) | $10^{-3}$ | $10^{-3}$ | $3 \times 10^{-6}$ | $3 \times 10^{-6}$ |
| $\tau_h$ (s) | $10^{-3}$ | $2 \times 10^{-3}$ | $2 \times 10^{-6}$ | $10^{-6}$ |
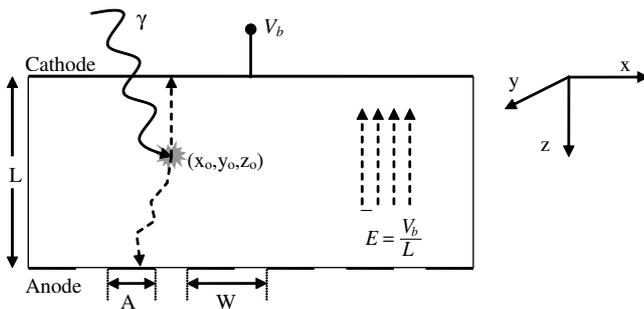


**Figure 1.** Cross-sectional detector configuration. The cathode electrode is connected to the negative biasing voltage $V_b$, while the anode pixels are held at ground voltage by a charge sensitive preamplifier (CSA).

Room temperature compound semiconductor materials, such as CdTe and CdZnTe, have numerous advantages as radiation detectors. However, they do not have the desired charge transport characteristics (eV Products 2006) similar to other semiconductor detectors, such as silicon (Si) or germanium (Ge) (Owens and Peacock 2004), as shown in table 1. Their poor hole transport is one of their most important drawbacks. To mitigate this hurdle, different structures such as strips (Hamel *et al* 1996) or pixels (Bennett *et al* 1997), have been proposed to enhance the signal induced by electrons moving close to the anode and to minimize the contribution of the holes. Due to charge trapping by impurities or defects, the total charge induced current no longer exclusively depends on the distance that carriers travel but also on their proximity to the sensing electrode (Eskin *et al* 1999) resulting in a pulse-height spectrum with a characteristic trapping tail. An important line of research attempts to optimize the detector geometries in order to improve the spectral properties of the detected signal by investigating and further developing strip (Cola *et al* 2001, Montemont *et al* 2007) and pixellated (Iwata *et al* 1999, Sowinska *et al* 2002, Qiang *et al* 2007) detectors to maximize efficiency and energy resolution.

This work aims at determining by simulation the optimum detector material and configuration in a wide energy range that goes from x-ray (10–40 keV) to PET imaging (511 keV). It is known that the optimum device configuration required to maximize the small pixel effect depends on the charge carriers transport characteristics, and therefore accurate simulations of the transport phenomena are required in order to find the best detector design.

Several researchers have dealt with the modelling of charge transport and induced currents in CdTe/CdZnTe semiconductor detectors. Heanue *et al* (1997) simulated radiation–matter interactions with the EGS4 Monte Carlo code (Nelson *et al* 1985); for each interaction the path of the charge carrier was computed and then a one-dimensional transport equation along this curved path was numerically solved. These simulations included the effects of both trapping and detrapping, significant inter-pixel spacing and non-linear electric field profiles and enabled the study of the small anode effect in relatively large strip detectors of various geometries. Prettyman (1999) implemented the numerical solution of the adjoint electron/hole continuity and Poisson equations to produce a 2D charge induction efficiency (CIE) map to compute the pulse-height spectrum. Finally, Picone *et al* (2003) used the adjoint equation concept to extend the planar model initially described in Glière *et al* (2000), to present an accurate method for determining the 3D distribution of charge pulses produced in a semiconductor incorporating models of electronic signal processing and electronic noise. These methods provide an accurate estimation of the induced charge and pulse shape but suffer from a high computational cost as a result of the need for numerically solving several differential equations.

This paper employs a 3D detector model that extends the approach pursued in Zumbiehl *et al* (2001) by incorporating a simplified Monte Carlo (MC) simulator that calculates gamma-ray energy deposition in the material and by integrating a more complete noise model to estimate the contribution of the different sources of noise for the different scenarios under consideration.

This work consists of three sections: first, the structure of the simulator is described, second, the scenarios simulated are presented and finally the results are given and conclusions are drawn. The results focus on estimating performance parameters such as energy resolution and efficiency in order to find the best possible compromise, while minimizing the intrinsic spatial resolution for different detector dimensions and transport properties.

## 2. Material and methods

### 2.1. Detector geometry

In this work the pixellated array geometry shown in figure 1 is considered. The top electrode is held at a constant biasing
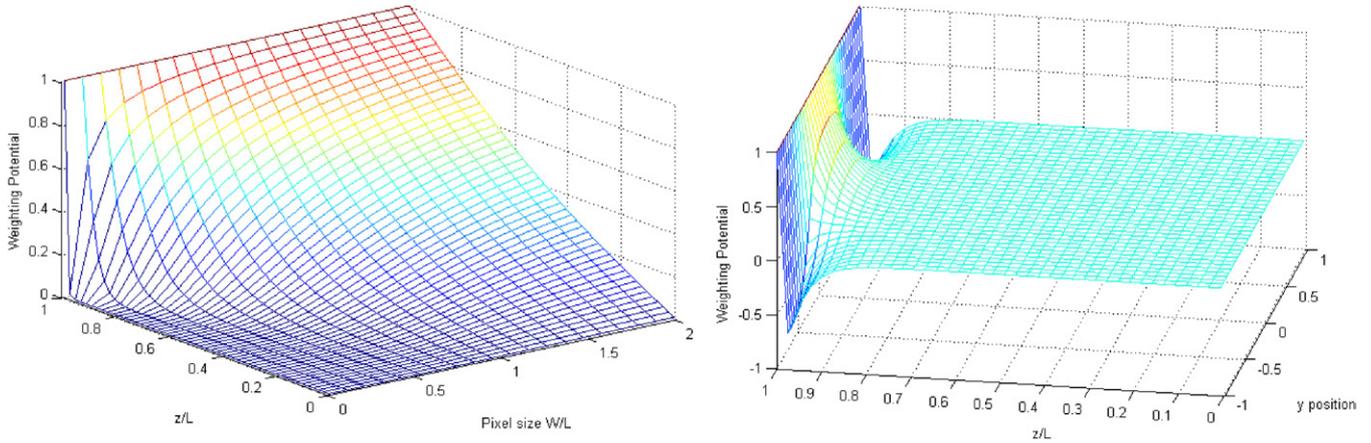
**Figure 2.** (Left) Anode weighting potential $\Phi_{\mathrm{w,a}}$ for pixel ratios between 1/100 and 2 and at depths ranging from 0 (cathode) to 1 (anode). (Right) Longitudinal section of the anode weighting potential $\Phi_{\mathrm{w,a}}$ $(x = 0,\, y,\, z)$ for a pixel ratio of $W/L = 0.2$ and $W = 1$.

potential $V_{\mathrm{b}}$ while the bottom anode pixels are kept at ground potential.

### 2.2. 'Pseudo-Monte Carlo' simulator

The implemented computer code simulates the gamma-ray–matter interactions and the generation of electron–hole pairs, whose end result (collection or trapping) is simulated for each charge carrier individually. Right through the document the electrons are denoted as $e$ and the holes as $h$. The simulator breaks down into the following seven steps:

1. *Photon interaction.* The first step consists of simulating radiation–matter interactions of gamma rays impinging into the CdTe/CdZnTe semiconductor materials. The simulator takes into account Compton scattering and photoelectric absorption but neglects pair production because conventional nuclear imaging modalities take place in gamma-ray energies below the pair-production energy level. Therefore, it can be assumed that inelastic scattering is the dominant process in the upper energy range of interest while photoelectric absorption plays a major role at lower energies.

The simplified MC simulator creates a list of hits for every gamma ray, comprising one or several Compton depositions and possibly a final photoelectric deposition. For each interaction the actual point $(x_0,\, y_0,\, z_0)$ and deposited energy $EN$ are recorded. Characteristic x-ray generation in the material after energy deposition is neglected as a first approach.

CdTe and CdZnTe cross section values between 10 keV and 1 MeV are taken from the photon cross section database of the National Institute of Standards and Technology (Berger *et al* 1998). In the case of a Compton interaction, the Klein–Nishina distribution (Davisson *et al* 1952) is sampled to determine the polar angle $\theta_{\mathrm{c}}$ of the scattered gamma ray, while the azimuthal angle $\varphi_{\mathrm{c}}$ is uniformly distributed between 0 and $2\pi$.

2. *Hole–electron pairs generation.* Each gamma-ray interaction implies the deposition of a given energy within the material, which in turn creates a cloud of thousands of electron–hole pairs. The actual number of pairs $N$ is considered to be a random number with Poisson statistics and is a function of the deposited energy $EN$ and the material properties. In the simulator, it is considered that the Poisson distribution converges to a Gaussian with median $\mu$ and variance $\sigma^2$ when $N$ is sufficiently large, as it is in our case:

$$N \sim G(\mu, \sigma^2) \begin{cases} \mu = \dfrac{EN}{w}, \\[2mm] \sigma^2 = F \cdot \dfrac{EN}{w}, \end{cases} \tag{1}$$

where $EN$ is the deposited energy, $w$ is the average electron–hole pair creation energy and $F$ is the Fano factor with values depending on the actual material; for CdZnTe and CdTe, F has a value between 0.1 and 0.2 (Lutz 1999).

Energy depositions are considered 'ideal' in the sense that subsequent x-ray and/or Auger electron emissions are neglected in this simplified computer model. However, this may be a limitation in the simulation of small pixels, whose energy resolution is prone to degradation due to the escape of K-shell x-rays, straggle of energetic electrons, Compton scattering and diffusion of charge carriers (Eskin *et al* 1999).

3. *Charge trapping.* Under the action of an electric field, charge carriers drift towards their collecting electrode and this movement induces current signals on the external electrodes. Each charge carrier either reaches its collecting electrode or is lost at some point along its trajectory, due to recombination or defect trapping. The carrier lifetime is a combination of recombination and defect trapping, both being inversely proportional to carrier concentration (Du *et al* 2003). Under low radiation, which is the case of medical nuclear imaging, trapping is the dominant factor (Guerra *et al* 2008).

The ultimate fate of the carrier depends on the material transport properties, detector dimensions and biasing voltage. Detrapping is neglected here. The actual lifetime $t_{\mathrm{h,e}}$, i.e. the time before charge trapping, of each charge carrier is a random variable $t$ that is drawn from an exponential distribution whose charge average lifetime is $\tau_{\mathrm{h}}$ for the holes and $\tau_{\mathrm{e}}$ for the electrons:

$$t_{\mathrm{h,e}} \sim \tau_{\mathrm{h,e}} \cdot \exp\left(-\frac{t}{\tau_{\mathrm{h,e}}}\right). \tag{2}$$
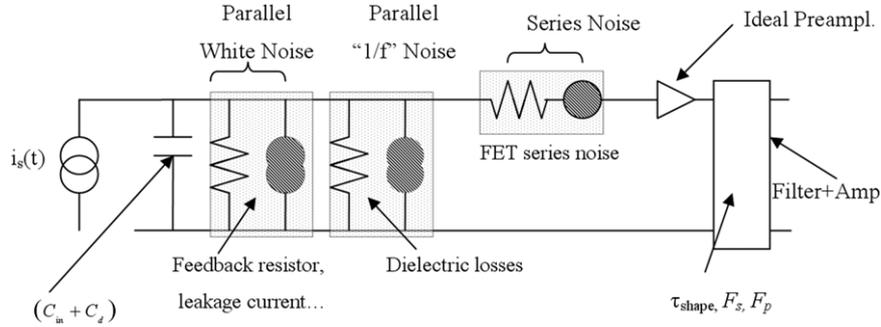
**Figure 3.** Basic noise sources in the detector–amplifier circuit.

**Table 2.** Electronics settings (Pettersen *et al* 2005).

| | |
|---|---|
| PreAmp transconductance $G_m$ (mS) | 3.5 |
| CSA feedback resistor $R_{fp}$ (GΩ) | 1 |
| CSA input capacitance $C_{int}$ (pF) | 2.5 |
| External capacitance $C_{ext}$ (pF) | 5 |
| First order CRRC shaping FP = FS | $e^2/8 = 0.92$ |
| Shaping time $\tau$ (μs) | 6 |
| ENC $e$ (RMS) | <250 |
| Dielectric capacitance (pF) | 1 |
| Dielectric loss factor | $10^{-4}$ |

As expressed in the following equation, the distance that can be covered by each charge carrier in $t_{h,e}$ is $d_{h,e}^z$ and if the survival time $t_{h,e}$ is sufficient for the carrier to reach an electrode, then the final point $z_{h,e}$ is either the anode, $z_e = 0$, or the cathode, $z_h = L$:

$$
\begin{aligned}
d_{h,e}^z &= E \cdot \mu_{h,e} \cdot t_{h,e} \qquad 0 < d_{h,e}^z < L, \\
z_e &= \max\left(z_0 - d_e^z, 0\right), \\
z_h &= \min\left(z_0 + d_h^z, L\right),
\end{aligned}
\tag{3}
$$

where $E$ is the electric field, $L$ is the material thickness, $t_{h,e}$ is the actual lifetime and $\mu_{h,e}$ are the hole/electron mobilities. In the case of a charge carrier reaching an electrode, the actual drift time $\breve{t}_{e,h}$ will be

$$
\begin{aligned}
\breve{t}_e &= \frac{z_0 - z_e}{E \cdot \mu_e}, \\
\breve{t}_h &= \frac{z_h - z_0}{E \cdot \mu_h}.
\end{aligned}
\tag{4}
$$

4. *Charge diffusion.* Usually, diffusion may be neglected in a first approximation since it can be considered that the diffusion length is negligible compared with typical pixel dimensions over the drift time. However, early experimental results (Malm *et al* 1975) lead to the conclusion that ignoring charge diffusion and the finite volume where the charge is created might be the source of discrepancies between theory and experimental measurements.

During its lifetime, each charge carrier diffuses laterally in the $(x, y)$ plane while travelling at a constant speed in the $z$ direction driven by the electric field (figure 1). Assuming a uniform electric field is certainly the worst approximation which is done here; however, it simplifies the modelling enabling the decoupling between the $x, y$ Brownian motion
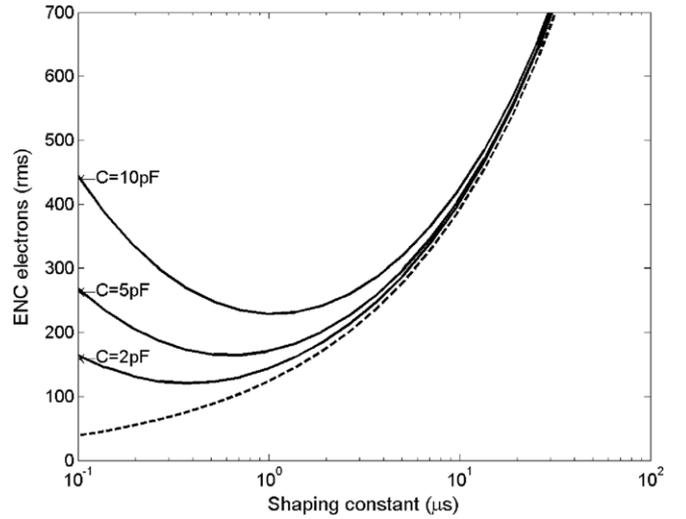


**Figure 4.** Estimated ENC for variable shaping time constants and detector capacitance of 2, 5 and 10 pF. The detector shot noise is plotted in dashed line to provide a reference.

**Table 3.** Material main properties (eV Products 2006) (Owens and Peacock 2004).

| | $Cd_{0.9}Zn_{0.1}Te$ | CdTe |
|---|---|---|
| Density (g cm$^{-3}$) | 5.78 | 5.85 |
| Resistivity (Ω cm) | $3 \times 10^{10}$ | $1.5 \times 10^{10}$ |
| Electron lifetime (s) | $3 \times 10^{-6}$ | $3 \times 10^{-6}$ |
| Hole lifetime (s) | $10^{-6}$ | $2 \times 10^{-6}$ |
| Dielectric constant | 10.9 | 11 |
| Pair creation energy (eV) | 4.64 | 4.43 |
| Electron mobility (cm$^2$ V$^{-1}$s$^{-1}$) | 1000 | 1100 |
| Hole mobility (cm$^2$ V$^{-1}$s$^{-1}$) | 50–80 | 100 |
| Fano factor | 0.1 | 0.14 |

and the charge transport in $z$. The diffusion distance $d^r$ along the radial axis is a function of the diffusion constant as follows:

$$
d_{h,e}^r \sim G\left(0, \sigma_{h,e}^2\right)
\begin{cases}
\sigma_{h,e}^2 = 2 \cdot D_{h,e} \cdot \min\left\{\breve{t}_{h,e}, t_{h,e}\right\}, \\
D_{h,e} = \frac{kT}{q}\mu_{h,e},
\end{cases}
\tag{5}
$$

where $k$ is the Boltzmann constant, $T$ is the temperature, $D_{h,e}$ are the diffusion constants for the electrons and holes given by the Einstein relation and $q$ is the electron charge. The diffusion
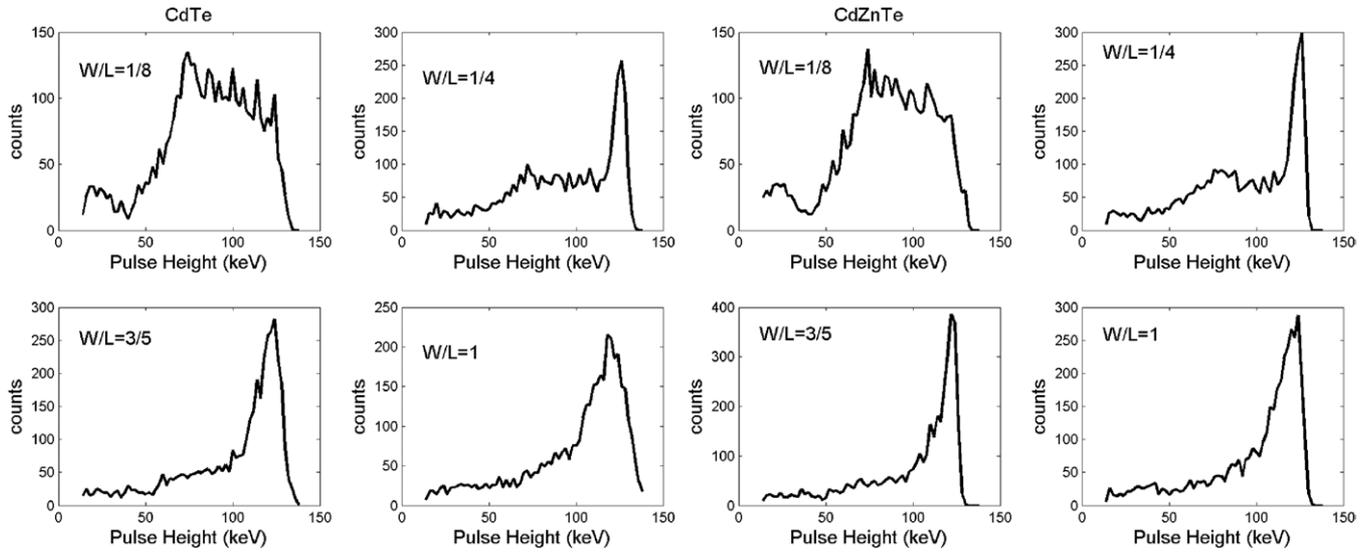
**Figure 5.** Estimated CdTe(left group) and CdZnTe (right group) pixel spectra at 140 keV for a 5 mm thick detector, nominal transport properties and biasing $V_b$ of $-400$ V.

time is considered as the minimum between the drift time, $\breve{t}_{e,h}$ and the carrier's actual lifetime, $t_{h,e}$. The final point of the electron e is $(x_e, y_e, z_e)$ and the hole $h$ is $(x_h, y_h, z_h)$, as shown in the following equation:

$$
\begin{aligned}
(x_e, y_e, z_e) &= \left(x_0 + d_e^r \cdot \cos\theta_e, y_0 \right. \\
&\quad \left. + d_e^r \cdot \sin\theta_e, \max(z_0 - d_e^z, 0)\right), \\
(x_h, y_h, z_h) &= \left(x_0 + d_h^r \cdot \cos\theta_h, y_0 \right. \\
&\quad \left. + d_h^r \cdot \sin\theta_h, \min(z_0 + d_h^z, L)\right),
\end{aligned}
\tag{6}
$$

where $\theta_e$ and $\theta_h$ represent the relative diffusion angle in the $(x, y)$ plane of the Brownian motion with respect to $(x_0, y_0)$ and they are considered as random variables uniformly distributed in $(0, \pi)$.

5. *Electrode charge induction*. When a charge carrier moves inside the detector, charge on each readout electrode is induced by electrostatic influence, and the induced charge, according to the Ramo–Shockley theorem (Ramo 1939), is represented by the weighting potential. This theorem provides a convenient way to calculate the current flowing through an electrode due to charge carrier motion and to explain the signals induced at the electrodes (Eskin *et al* 1999). The theorem states that the induced charge at the anode $Q_a$ can be computed as the difference between two weighting potentials (He 2001). In this way $N$ individual charge carriers induce a charge $Q_a$ in the anode and $Q_c$ in the cathode that are related to the difference of the weighting potentials at each electron and hole end points, $(x_e, y_e, z_e)$ and $(x_h, y_h, z_h)$, respectively:

$$
\begin{aligned}
Q_a &= \sum_N \Phi_{w,a}(x_e, y_e, z_e) - \Phi_{w,a}(x_h, y_h, z_h), \\
Q_c &= \sum_N \Phi_{w,c}(x_e, y_e, z_e) - \Phi_{w,c}(x_h, y_h, z_h).
\end{aligned}
\tag{7}
$$

The weighting potentials for the anode $\Phi_{w,a}$ and cathode $\Phi_{w,c}$ are derived from the three-dimensional analytical solution of

the Laplace equation described in (Castoldi *et al* 1996), whose value can be computed for variable pixel aspect ratios, as shown in figure 2. The left plot shows the weighting potential function $\Phi_{w,a}$ along the pixel's central axis from cathode ($z = 0$) to anode ($z = 1$) for aspect ratios ($W/L$) between 0 and 2. When the pixel length $L$ is much bigger than the pixel size ($W$), i.e. $L \gg W$, $\Phi_{w,a}$ is not zero only at points very close to the anode, a phenomenon known as 'small pixel effect'. On the other hand $\Phi_{w,a}$ is linear when pixel size and detector thickness are of the same order.

As an example, for an electron generated at $(x_e, y_e, z_e)$ due to an energy deposition and having lifetime long enough to reach the anode, where $\Phi_{w,a} = 1$, i.e. the electron does not suffer any trapping, and considering that electrons are much faster than holes, the induced charge is approximately:

$$
Q_a = 1 - \Phi_{w,a}(x_e, y_e, z_e).
\tag{8}
$$

Since the weighting potential $\Phi_{w,a}$, shown in figure 2(right), depends on the position, the previous simplified equation explains why the charge and current induced at the anode depend on the interaction point $(x_0, y_0, z_0)$. Moreover, the equation also explains the characteristic tail of pulse height spectra of CdTe and CdZnTe.

6. *Hit fusion*. Each simulated gamma ray interacts several times within the semiconductor material at different points $(x_0, y_0, z_0)^i$, and a list of hits is generated consisting of a sequence of Compton interactions and a possible final photoelectric interaction. At each interaction point an energy $EN^i$ is deposited. Each energy deposition generates a random number $N^i$ of charge carriers that drift towards the electrodes inducing the readout charges $Q_a^i$ and $Q_c^i$.

The hit fusion module includes the total induced charge as the summation of the $i$ partial contributions. Timing effects, such as pulse pile-up or device polarization due to charge build-up, are neglected because these are not significant under low photon flux, which is the case in nuclear imaging applications.
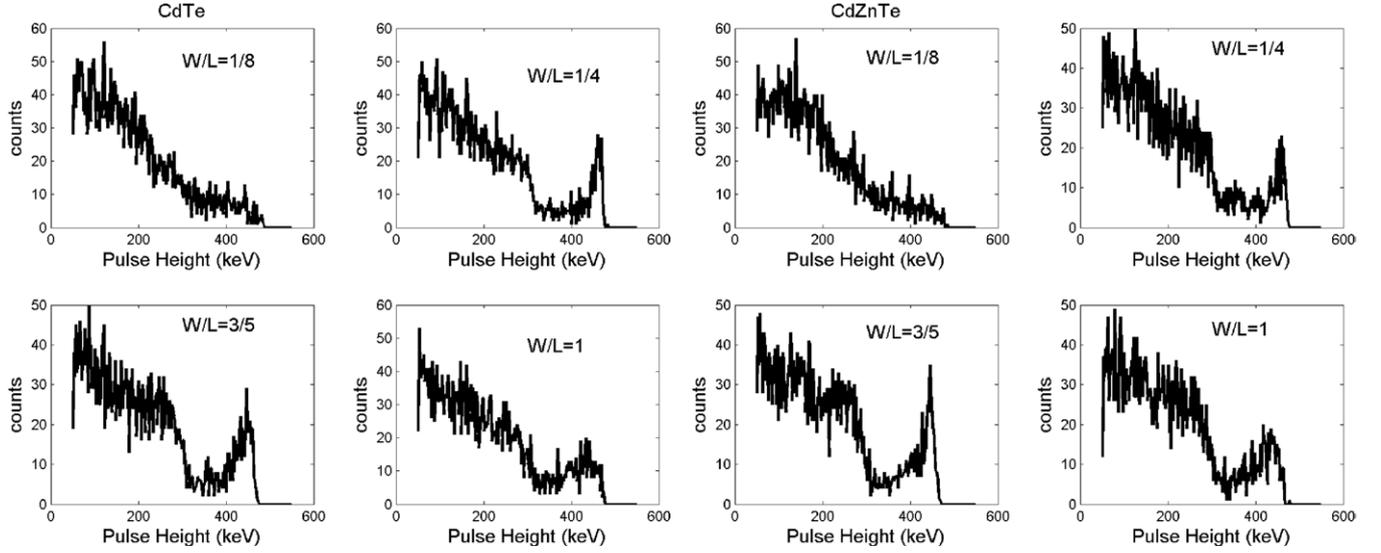
**Figure 6.** Estimated CdTe pixel (left group) and CdZnTe (right group) spectra at 511 keV for a 5 mm thick detector, nominal transport properties and biasing $V_b$ of $-400$ V.

7. *Noise considerations*. Signal distortion by noise is inherent to detection and amplification stages, and its origins and implication have been widely studied (Radeka 1988). Two main noise sources are considered: the detector, mainly due to the leakage current, and the electronics, mainly due to the low-noise preamplifier and the feedback resistors, as shown in figure 3. These two noise sources contribute to the total mean equivalent noise charge (ENC) as the sum of different white and/or pink parallel and series inputs (Radeka 1988):

$$\mathrm{ENC}^2 = \mathrm{ENC}^2_{\mathrm{PREAMP}} + \mathrm{ENC}^2_{\mathrm{DETECTOR}}. \qquad (9)$$

In the preamplifier, we take into account the loading capacitances, including the detector capacitance $C_d$, the preamplifier input capacitance $C_{in}$, the shaping time constant of the filters $\tau_{\mathrm{shape}}$, the transconductance of the preamplifier transistor $g_m$, the feedback resistor value $R_p$, the preamplifier bias current $I_{dc}$ and other coloured noise contributions, which are proportional to the load and parasitic capacitances.

$$\mathrm{ENC}^2_{\mathrm{PREAMP}} = \begin{cases} \dfrac{F_s}{\tau_{\mathrm{shape}}} \cdot \dfrac{4kT}{q^2} \dfrac{2}{3g_m} \left(C_{in} + C_d\right)^2 + \cdots, \\[2ex] F_p \tau_{\mathrm{shape}} \cdot \left( \dfrac{4kT}{q^2} \dfrac{1}{R_p} + \dfrac{2I_{dc}}{q} \right) + \mathrm{ENC}^2_{1/f}, \end{cases}$$

$$\mathrm{ENC}^2_{1/f} \approx K_{1/f} \left( \frac{C^2_{\mathrm{total}}}{C_{GS}} + 2C_{\mathrm{total}} + C_{GS} \right), \qquad (10)$$

where $F_s$ and $F_p$ are the series and parallel form factors for the readout filters, $K_{1/f}$ is a proportionality factor, $C_{GS}$ is the preamplifier gate–source capacitance, $C_{\mathrm{total}}$ is the total loading capacitance, $q$ is the electron charge, $k$ is the Boltzmann
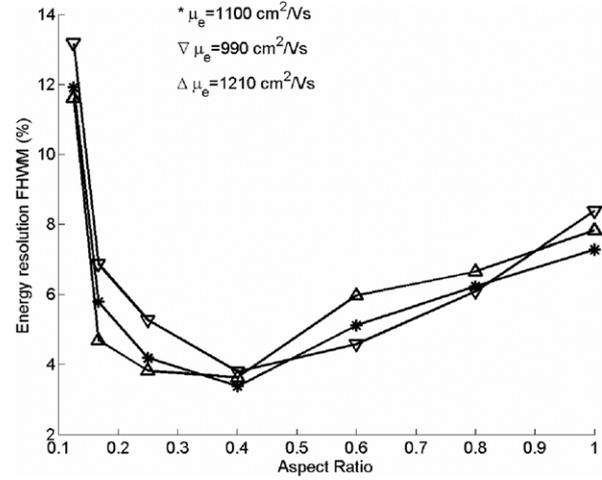


**Figure 7.** Estimated energy resolution FHWM for CdTe at 140 keV with W/L between 0.1 and 1 and nominal (*) transport properties as well as 10% below ($\triangle$) and 10% above ($\nabla$).

constant and $T$ is the temperature:

$$\mathrm{ENC}^2_{\mathrm{DETECTOR}} = \mathrm{ENC}^2_{\mathrm{PARALLEL}"f"} + \mathrm{ENC}^2_{\mathrm{PARALLELWHITE}},$$

$$\mathrm{ENC}^2_{\mathrm{PARALLELWHITE}} = 2 \cdot F_p \cdot \frac{I_{\mathrm{leak}} \cdot \tau_{\mathrm{shape}}}{q}, \qquad (11)$$

$$\mathrm{ENC}^2_{\mathrm{PARALLEL}"f"} \approx \frac{6}{10} \frac{4kT}{q^2} D \cdot C_\varepsilon,$$

where $I_{\mathrm{leak}}$ is the leakage current, $C_\varepsilon$ is the dielectric capacitance and $D$ is the dielectric loss factor, which is equal to the imaginary part of the permittivity and is independent of the frequency in the range of interest.

Due to biasing, leakage current flows through the detector, which may be considered as a fully depleted negatively biased diode. However, the way this leakage current $I_{\mathrm{leak}}$ contributes to the noise is in question. It has been shown that surface leakage currents do not generate significant shot noise, and
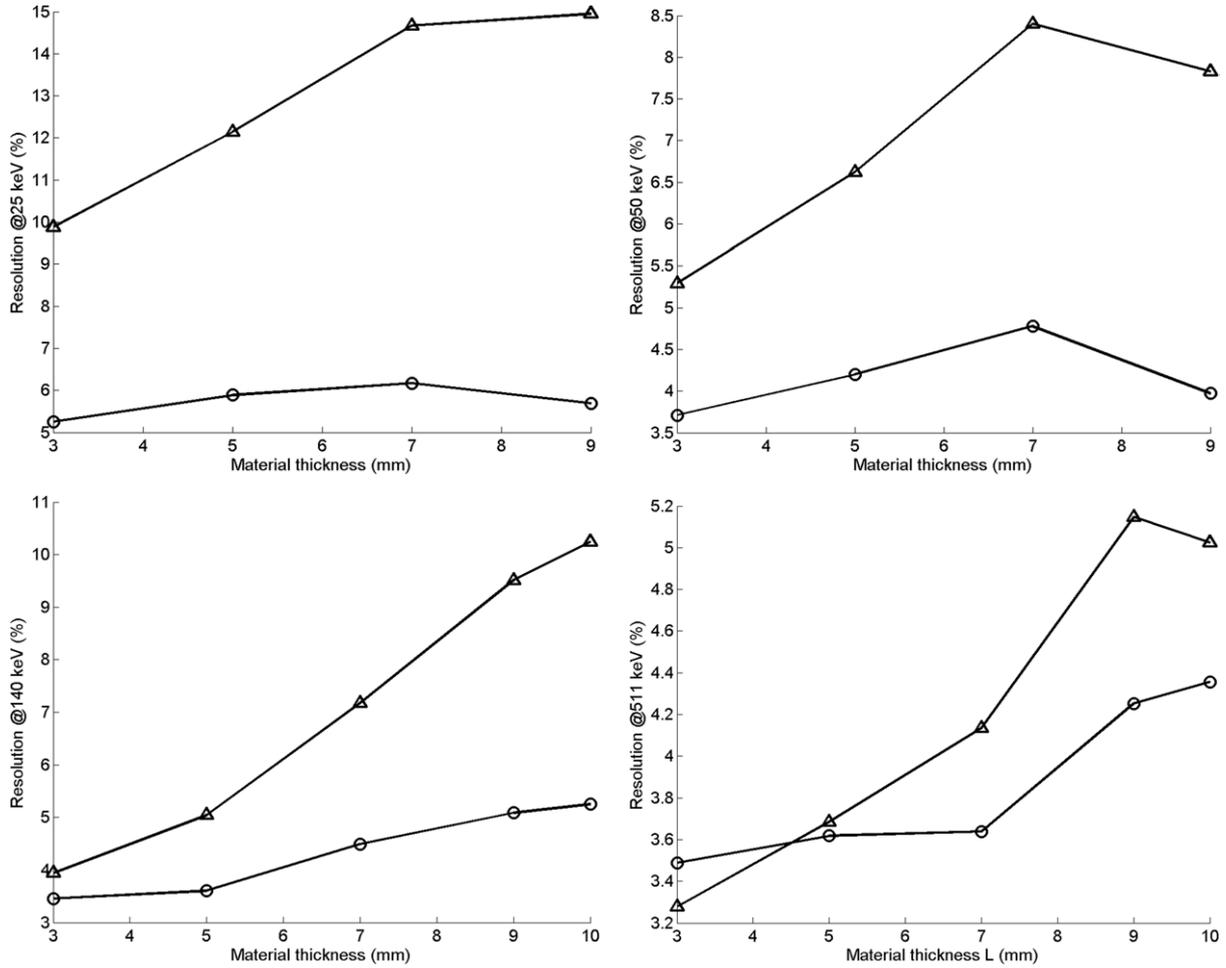
**Figure 8.** CdTe(△) and CdZnTe(o) maximum energy resolution at 25, 50, 140 and 511 keV for crystal thickness *L* between 3 and 10 mm.

therefore, only bulk leakage currents contribute to the noise through the ENC$_{\text{PARALELWHITE}}$ noise term. Moreover, it has been demonstrated that the actual parallel noise is only a fraction of the shot noise generated by the bulk current (Luke *et al* 2001).

These experimental findings can be explained if we take into consideration the detector readout contacts. It has been shown that the bulk current highly depends on the selected anode contact material (Scyoc *et al* 2001): gold usually forms Schottky contacts, while indium or platinum form ohmic contacts. In the non-ohmic contact case, the bulk current is limited by the creation of Schottky barriers in the readout pad (Luke *et al* 2002), and therefore, the *I*–*V* curve of the detector is similar to the one of a highly nonideal diode in series with a large resistor (the bulk CZT). The rectifying metal-semiconductor junction can be described by the standard diode equation:

$$I = A \cdot J_{\text{o}} \cdot (\exp{(V_{\text{b}}/n \cdot V_{\text{thermal}})} - 1),$$
$$V_{\text{thermal}} = \frac{k \cdot T}{q}, \tag{12}$$

where *A* is the pixel size, $J_0$ is the diode reverse saturation current density, *k* is the Boltzmann constant, *T* is the temperature and *n* is the ideality factor, which in the case of

CZT is assumed to be between 1.07 and 1.13 (Cordes and Schmid-Fetzer 1994).

## 3. Results

The pseudo simulator that implements the equations described in the previous section was realized with Matlab 7.1 (Mathworks, Natick, MA, USA).

The results are divided into two phases. First, the electronics descriptions and results provided in (Pettersen *et al* 2005) and summarized in table 2 are employed to fit the noise model given by equation (9). The proportionality $K_{1/f}$ factor in ENC$_{1/f}$ is computed to account for the fact that in an ASIC the preamplifier noise is dominated by flicker noise. After the inclusion of the $1/f$ noise factor, the model predicts an ENC that increases linearly with the external capacitance $C_{\text{ext}}$. For instance the predicted ENC is 85e+11*e*/pF when the shaping constant $\tau$ is 10 $\mu$s, a value that very well matches the reported measured electronic noise of 56e+11.6*e*/pF and the experimental base level noise of 85 eV (Pettersen *et al* 2005).

The ENC values shown in figure 4 were computed for shaping constants between 100 ns and 50 $\mu$s, external detector capacitances of 2, 5 and 10 pF and a bulk current of
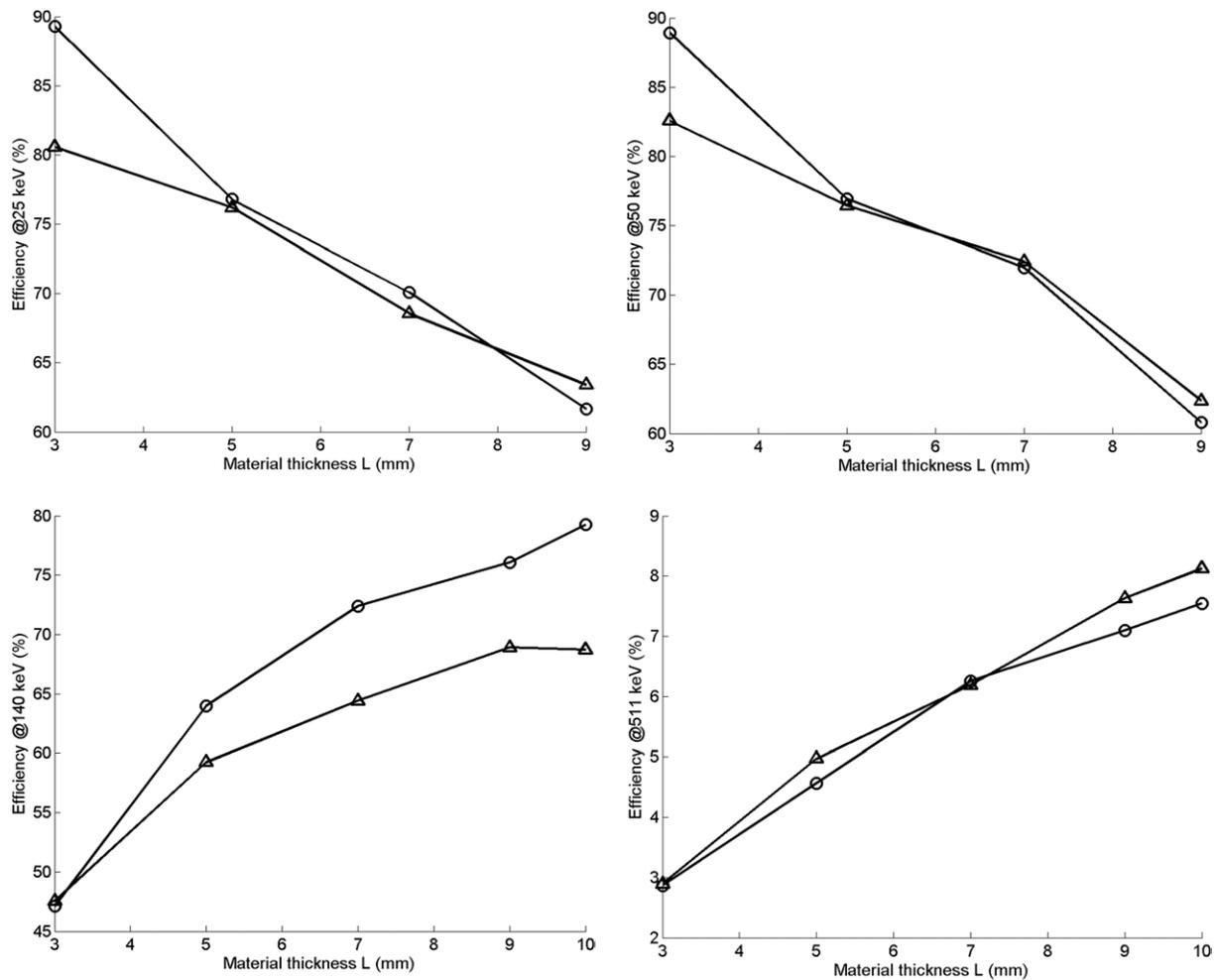
**Figure 9.** CdTe($\triangle$) and CdZnTe(o) maximum efficiency at 25, 50, 140 and 511 keV for crystal thickness *L* between 3 and 10 mm.

250 pA/pixel, which is consistent with leakage measurements published in (Dirks *et al* 2006). For the simulated scenario, as shown in figure 4, ENC is estimated to be lower than 250 *e* (rms).

The pixel performance was simulated for CdTe and CdZnTe, with the material properties summarized in table 3, for 5000 incident $\gamma$-rays at 25, 50, 140 and 511 keV for detectors 3, 5, 7 and 10 mm thick and aspect ratios W/L between 0.125 and 1. For each combination nominal transport properties, as well as values 10% above and below the nominal ones, were considered. The simulations estimated the equivalent noise level for each setup, based on equations as given in the previous section, ranging between 150 and 250 eV depending on the material properties and pixel dimensions. For each thickness the material bias is modified to obtain a nominal electric field of 1000 V cm$^{-1}$.

In total, about $2 \times 10^6 \gamma$-rays were simulated and a computation time equivalent to 320 days in a single 2.4 GHz Pentium Core2 6600 was required. The aim of these simulations was to determine the optimum detector setup for a CZT/CdTe-based medical imaging scanner operating within a wide range of energies.

As an example, figure 5 shows the simulated results for CdTe/CdZnTe, respectively, with different aspect ratios and

140 keV incident gamma rays. Additionally, figure 6 exhibits the results for the same scenario as before but with 511 keV indicent gamma rays. The peak of these plots corresponds to the excitation energy (511 or 140 keV), while the tail is the combination of Compton scattering and the dependence of the detector efficiency on the depth of interaction.

For the given transport properties the best energy resolution of CdTe is obtained at $W/L = 0.25$, as demonstrated in figure 7. With these plots, it becomes evident that there is an optimum ratio that maximizes energy resolution, which varies with the material and the gamma energy, as shown in figure 8. The energy resolution is computed as the FWHM of the Gaussian fit at the photopeak.

So far, the plots represent results with nominal transport values; however, in order to account for material deviations from these nominal values, the analysis that follows will average simulation outputs with nominal transport values and nominal ±10%.

The primary reason for investigating solid-state detectors for Nuclear Medicine is their potential to offer improved energy resolution over traditional scintillators, and thus provide superior Compton scatter rejection; for example at 140 keV a value of 3–4 keV (2–3%) FWHM would reduce the scatter component of the image reconstruction error to a level below

8
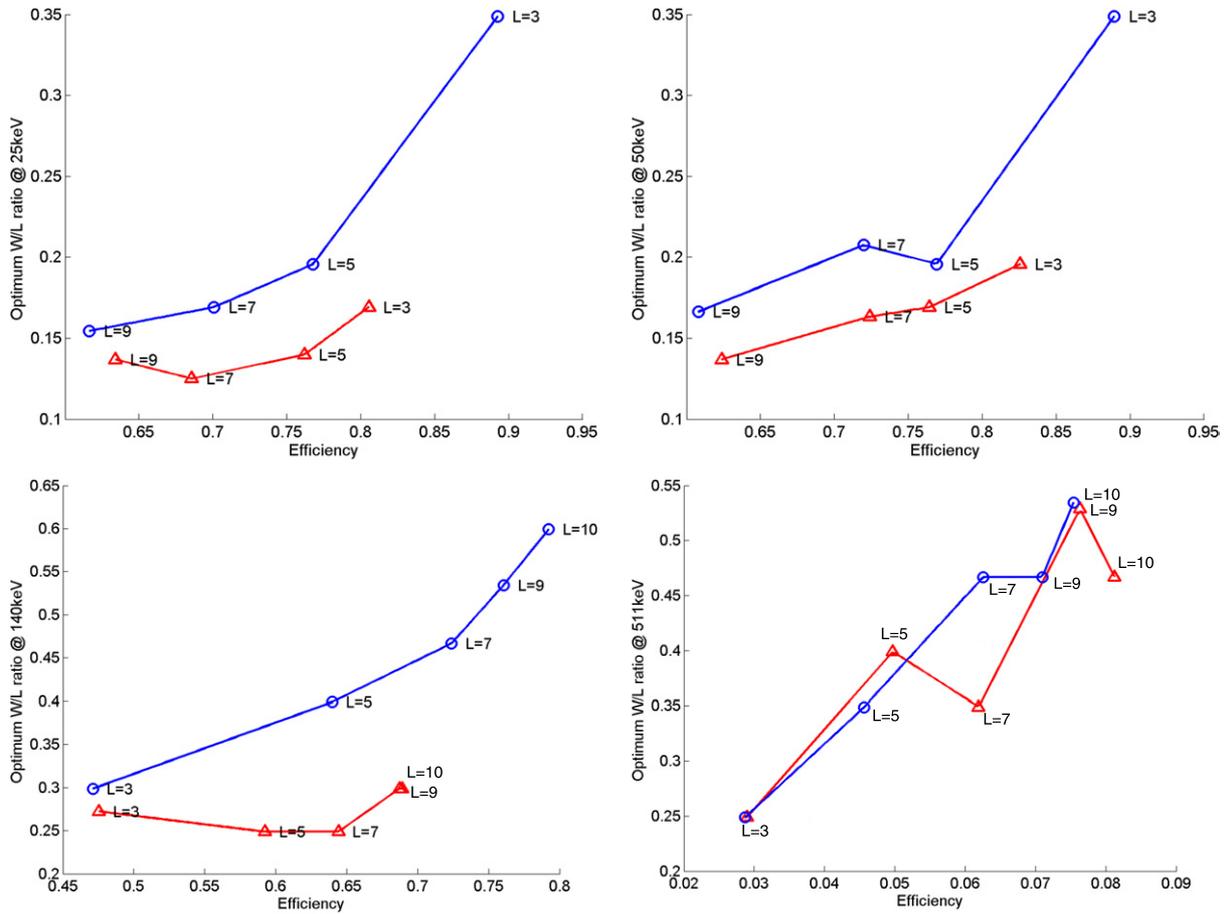
**Figure 10.** Optimum pixel ratio and efficiency for CdTe ($\Delta$) and CdZnTe(o) for crystal thickness $L$ of 3, 5, 7, 9 and 10 mm.

that of the photon statistics when using $^{99m}$Tc (Bennett *et al* 1997), yet, a more relaxed constraint of 5% FWHM resolution will be imposed, which is still far below that achievable with scintillators. The resolution is automatically computed as the FWHM around the photopeak. It is shown (figure 8) that, for the considered material properties in table 3, CdZnTe (o) provides higher energy resolution than CdTe ($\Delta$) at low energies. These performance figures can still be improved with biparametric techniques (Verger *et al* 2004) which aim at compensating the lower CIE close to the anodes. Figure 8 shows that a 5% restriction on energy resolution rules out the use of CdTe at room temperature in the low energy range, due to the excessive noise because of its lower bulk resistivity, but suggests a slightly better performance of CdTe at high energies.

Further, the imaging system is designed for being used in a wide range of energies where the detector should be able to stop a significant amount of x- and gamma rays in order to keep the patient dose as minimal as possible. Therefore, the sensitivity, which is computed as the fraction of hits whose energy is above the Compton edge, is required to be as high as possible, for example, above 75% for x-rays, 65% at 140 keV and as high as possible at 511 keV.

Figure 9 presents the sensitivity, i.e. detection efficiency, for crystals between 3 and 10 mm thickness when energy resolution is maximized. The efficiency is computed as the fraction of detected events with a detected energy above the

Compton edge. At low energies, most gamma rays interact very close to the cathode, and therefore any additional detector thickness degrades sensitivity by introducing more noise. On the other hand, at high energies most interactions are Compton, and therefore thicker detectors provide higher sensitivity. It is demonstrated that at low energies CdZnTe (o) provides slightly higher efficiency than CdTe ($\Delta$) while at PET energies both materials have comparable performance.

The previous results may be represented as bi-dimensional plots of the optimum pixel ratio versus efficiency when energy resolution is maximized, as shown in figure 10. These plots show that at low energies and for a given thickness CdZnTe will provide higher efficiency, while at 511 keV the performance of both materials is very much the same. However, there is a final parameter that needs to be minimized, which is the pixel pitch in order to provide the highest possible intrinsic spatial resolution. Figure 11 analyses the data from a different perspective; instead of maximizing the energy resolution, the pixel pitch is minimized provided a 5% energy resolution is secured.

The analysis of all these plots combined with design restrictions suggests a pixellated CdZnTe detector with a thickness of around 6 mm and a 1 mm pitch. In this case, according to these simulation results, the spatial resolution is maximized at high energies and the energy resolution is maximized at low energies, while a reasonable detection efficiency is achieved at high energies.
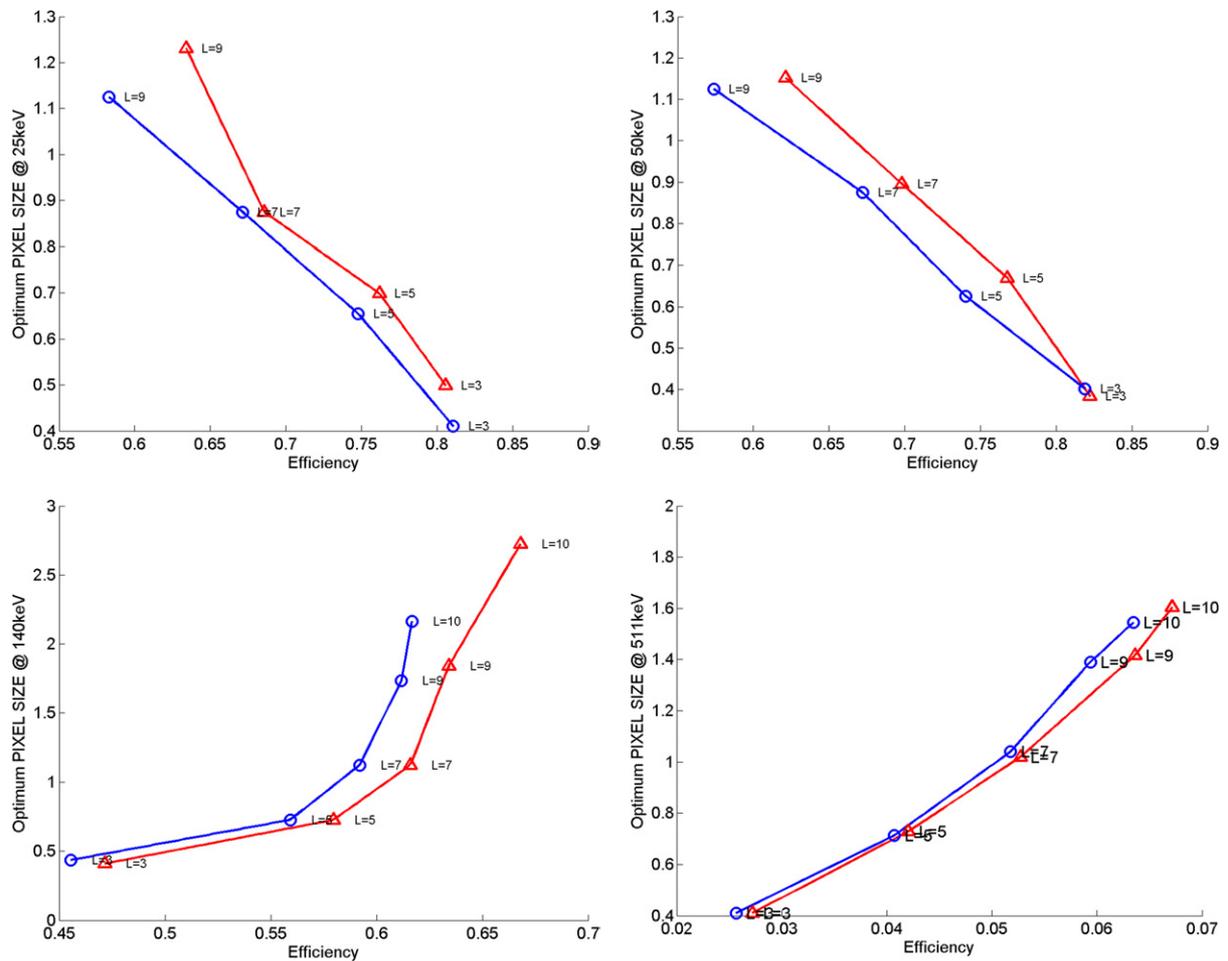
**Figure 11.** Efficiency and minimum pixel size in mm for CdTe (△) and CdZnTe(o) to sustain an energy resolution below 5% for crystal thickness $L$ of 3, 5, 7, 9 and 10 mm.

## 4. Conclusions and future work

This work has set up the simulation framework for the optimization of a pixellated room-temperature semiconductor detector for a medical imaging system that covers a wide range of energies, with a special focus on the accurate modelling of the noise sources, whose parameters were adjusted to reproduce experimental measurements reported in the literature for an existing readout ASIC.

The resulting model was used to estimate the pixel energy spectrum of CdTe and CdZnTe detectors with a resistive readout for four different energies, which are of interest in medical imaging, with different thickness to pixel ratios and transport mobility properties. Under the considered conditions, the simulation results demonstrated the superiority of the CdZnTe over the CdTe in terms of energy resolution and sensitivity in the photopeak. Finally, the simulations provided possible design specifications of a semiconductor imaging detector suitable to operate within a wide energy range, from 25 to 511 keV. According to the results, the spatial resolution is maximized at high energies and the energy resolution at low energies, while a reasonable detection efficiency is achieved at high energies, with a $1 \times 1 \times 6\,\text{mm}^3$ CdZnTe pixellated detector.

Future work will include an accurate and detailed model of photon interactions in the semiconductor crystal using GEANT4; extensive FEM analysis to predict the optimum detector performance including temporal response; and modelling of various overall imaging system architectures based on optimized detectors. Experiments will also be carried out with CdZnTe devices by eV Products with the appropriate specifications to further evaluate our simulation results.

## Acknowledgments

# References

Bennett P R *et al* 1997 High efficiency pixellated CdTe detector *Nucl. Instrum. Methods* A **392** 260–3

Berger M J *et al* 1998 *XCOM: Photon Cross Sections Database*. NIST Standard Reference Database 8 (XGAM) (http://physics.nist.gov/PhysRefData/Xcom/Text/XCOM.html)

Castoldi A *et al* 1996 Three-dimensional analytical solution of the Laplace equation suitable for semiconductor detector design *IEEE Trans. Nucl. Sci.* **43** 256–65

Cola A *et al* 2001 Simulation of the collection properties of CdTe strip detectors *IEEE Trans. Nucl. Sci.* **48** 292–5

Cordes H and Schmid-Fetzer R 1994 The role of interfacial reactions in Pt/CdTe contact formation *Semicond. Sci. Technol.* **9** 2085–96

Davisson C M *et al* 1952 Gamma-ray absorption coefficients *Rev. Mod. Phys.* **24** 79–107

Dirks B P F *et al* 2006 Leakage current measurements on pixelated CdZnTe detectors *Nucl. Instrum. Methods* A **567** 145–9

Du Y *et al* 2003 Temporal Response of CZT detectors under intense radiation *IEEE Trans. Nucl. Sci.* **50** 1031–5

Eisen Y and Shor A 1998 CdTe and CdZnTe materials for room-temperature X-ray and gamma ray detectors *J. Cryst. Growth* **184–185** 1302–12

Eskin J D *et al* 1999 Signals induced in semiconductor gamma-ray imaging detectors *J. Appl. Phys.* **85** 647–59

eV Products 2006 Material properties and http://www.evproducts.com/material_prop.pdf

Funaki M *et al* 1999 Growth and characterization of CdTe single crystals for radiation detectors *Nucl. Instrum. Methods* A **436** 120–6

Glière A *et al* 2000 Simulation of CdZnTe gamma-ray spectrometer response *Nucl. Instrum. and Methods Phys. Res. A: Accel. Spectrom. Detectors Associated Equipment* **442** 250–4

Guerra P *et al* 2008 Development of a simplified simulation model for performance characterization of a pixellated CdZnTe multimodality imaging system *Phys. Med. Biol.* **53** 1099–113

Hamel L A *et al* 1996 Signal generation in CdZnTe strip detectors *IEEE Trans. Nucl. Sci.* **43** 1422–6

He Z 2001 Review of the Shockley–Ramo theorem and its application in semiconductor gamma-ray detectors *Nucl. Instrum. Methods Phys. Res.* A **463** 250–67

Heanue J A *et al* 1997 Two-dimensional modeling of Cd(Zn)Te strip detectors *IEEE Trans. Nucl. Sci.* **55** 701–7

Iwata K *et al* 1999 CdZnTe detector for combined X-ray CT and SPECT *Nucl. Instrum. Methods* A **422** 740–4

Johnson C J *et al* 1993 Crystallographic and metallurgical characterization of radiation detector grade cadmium telluride materials *Spring Meeting of the Materials Research Society (San Francisco, CA)* p 463

Li L *et al* 2003 Development of a large single crystal (3-inch ingot) CdZnTe for large volume nuclear radiation detectors *SPIE Proc. Ser.* **4784** 76–83

Luke P N *et al* 2001 Noise in CdZnTe detectors *IEEE Trans. Nucl. Sci.* **48** 282–6

Luke P N *et al* 2002 Noise reduction in CdZnTe coplanar-grid detectors *IEEE Trans. Nucl. Sci.* **49** 1950–3

Lutz G 1999 *Semiconductor Radiation Detectors* (Berlin: Springer)

Malm H L *et al* 1975 Gamma–ray spectroscopy with single-carrier collection in high-resistivity semiconductors *Appl. Phys. Lett.* **26** 344–6

Montemont G *et al* 2007 Simulation and design of orthogonal capacitive strip CdZnTe detectors *IEEE Trans. Nucl. Sci.* **54** 854–9

Nelson W R *et al* 1985 EGS4 code system. Stanford Linear Accelerator Center, Menlo Park, CA, USA

Owens A and Peacock A 2004 Compound semiconductor radiation detectors *Nucl. Instrum. Methods* A **531** 18–37

Palosz W *et al* 1995 Experimental studies on mass transport of cadmium–zinc telluride by physical vapor transport *J. Cryst. Growth* **148** 56–62

Pettersen D M *et al* 2005 A readout ASIC for SPECT *IEEE Trans. Nucl. Sci.* **52** 764–71

Picone M *et al* 2003 A three-dimensional model of CdZnTe gamma-ray spectrometer *Nucl. Instrum. Methods Phys. Res. A: Accel. Spectrom. Detectors Associated Equipment* **504** 313–6

Prettyman T H 1999 Method for mapping charge pulses in semiconductor radiation detectors *Nucl. Instrum. Methods Phys. Res. A: Accel. Spectrom. Detectors Associated Equipment* **422** 232–7

Qiang L *et al* 2007 Test of CZT detectors with different pixel pitches and thicknesses *IEEE Nuclear Science Symp. (Honolulu, HI)* pp 2381–5

Radeka V 1988 Low-noise techniques in detectors *Annu. Rev. Nucl. Part. Sci.* **38** 217–77

Raiskin E and Butler J F 1988 CdTe low level gamma detectors based on a new crystal growth method *IEEE Trans. Nucl. Sci.* **35** 81–4

Ramo S 1939 Currents induced by electron motion *Proc. IRE* **27** 584–5

Scyoc J M V *et al* 2001 Further investigation of the operation of $Cd_{1-x}Zn_xTe$ pixel array detectors *Nucl. Instrum. Methods* A **458** 310–8

Sowinska M *et al* 2002 Spectral characteristics of small- and large-volume CdTe detectors: comparison among hemispheric, planar, and pixellated structure *IEEE Trans. Nucl. Sci.* **49** 3306–13

Szeles C 2004 Advances in the crystal growth and device fabrication technology of CdZnTe room temperature radiation detectors *IEEE Trans. Nucl. Sci.* **51** 1242–9

Szeles C and Eissler E E 1998 Current issues of high-pressure Bridgman growth of semi-insulating CdZnTe *Mater. Res. Soc.* **487** 3–12

Verger L *et al* 2004 Performance and perspectives of a CdZnTe-based gamma camera for medical imaging *IEEE Trans. Nucl. Sci.* **51** 3111–7

Zumbiehl A *et al* 2001 Modelling and 3D optimisation of CdTe pixels detector array geometry—extension to small pixels *Nucl. Instrum. Methods* A **469** 227–39